ANALYSIS OF BLADE'S CHORD LENGTH WITH NACA0015 PROFILE FOR ENHANCED WAVE ENERGY CONVERSION OF WELLS TURBINE

Kha Tuan Tran Huynh[1,2], Khoa Anh Vo[1,2], Vay Siu Lo[1,2], Thien Tich Truong[1,2,*]

[1]*Department of Engineering Mechanics, Faculty of Applied Sciences,
Ho Chi Minh City University of Technology (HCMUT), 268 Ly Thuong Kiet Street,
District 10, Ho Chi Minh City, Vietnam*
[2]*Vietnam National University Ho Chi Minh City, Linh Trung Ward,
Thu Duc City, Ho Chi Minh City, Vietnam*
*E-mail: tttruong@hcmut.edu.vn

Abstract. This paper investigates the enhancement of Wells turbine blades by modifying the chord length design parameter. The Wells turbine, a promising device in wave energy conversion systems, faces a limited operating range due to flow separation, which restricts its efficiency at higher flow rates. Enhancing the performance of the Wells turbine is crucial for effective wave energy exploitation. The computational simulations in this study are conducted using ANSYS Fluent. Turbine performance is evaluated based on non-dimensional torque, pressure torque, and efficiency, derived from solving the steady 3D incompressible Reynolds Averaged Navier–Stokes equations. The results are validated against reliable references, showing good agreement. The numerical findings reveal that altering the turbine chord length significantly impacts efficiency. Optimizing the chord length enhances the Wells turbine's performance in wave energy conversion, making it a more viable option for renewable energy power generation.

Keywords: wave energy conversion, Wells turbine, chord length, ANSYS fluent.

1. INTRODUCTION

To reduce dependence on energy sources such as oil, natural gas, coal, etc., there is a need to use energy that can be exploited and developed sustainably. In addition to renewable energy sources like solar and wind, energy from the sea is not to be missed.

The generation of energy by marine-based systems is more advantageous than the generation of energy from wind, as stated in reference [1]. Besides, residents near the coast can reduce their dependence on the national electricity system. Countries with extensive coastlines like England, India, Australia, and the United States are at the forefront of developing wave energy systems [2,3]. To harness wave energy, it has to be turned into electrical power through a system, depicted in Fig. 1, this system is known as the Oscillating Water Column (OWC) potential conversion system. This method is one of the most advanced technologies currently in use [4]. This OWC system has a plenum chamber containing a defined amount of air, and the air inside the chamber is directed to where the turbine is installed through a duct. The internal chamber pressure fluctuates as the water surface shifts due to wave action. These pressure variations cause the air inside the chamber to flow back and forth, creating a two-directional airflow. This airflow drives a self-rectifying turbine, allowing it to generate power from both airflow directions. In essence, the system transforms wave energy into mechanical energy, with air serving as the working fluid [5].
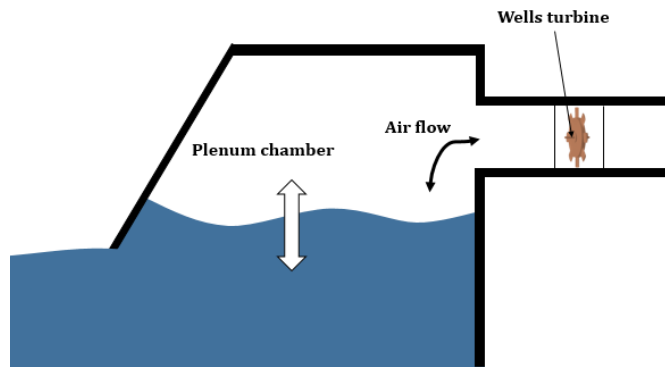

Fig. 1. Schematic demonstration of an OWC system matched with the Wells turbine

Wells turbine [5] is widely used in wave energy conversion systems, particularly in oscillating water column (OWC) devices. Turbine Wells is particularly suited for OWC applications due to its ability to rotate in a fixed direction regardless of the airflow direction. The OWC system operates based on the principle of converting the up-and-down motion of ocean waves into oscillating compressed air within a chamber. Turbine Wells, located within this air chamber, is driven by the oscillating compressed air. Due to its unique symmetrical blade structure, the turbine generates torque in a single direction, regardless of the airflow direction [6,7]. The design of Turbine Wells consists of key components such as symmetrical turbine blades, arranged at a 90-degree offset angle to the rotor axis, with the commonly used NACA 00XX airfoil profile [5,6]. Turbine Wells may or may not have guide vanes, which are positioned on both sides of the rotor to recover the swirling energy from the outgoing air, thus improving the turbine's efficiency.

The rotor configurations of Turbine Wells are diverse, including monoplane, biplane, and contra-rotating rotors. Turbine Wells offer several advantages, such as simple construction, low manufacturing costs, and relatively high efficiency, with peak efficiency reaching up to approximately 75%. The system also exhibits linear characteristics, where pressure decreases proportionally with airflow at constant rotational speed. As illustrated in Fig. 2, this design ensures optimal performance and reliability, making the Wells turbine a prominent choice in wave energy conversion technologies [6,7].

Additionally, the blades of the Wells turbine are aligned at a 0-degree angle to the rotational plane around the hub. One of its main advantages is simplicity, making it an ideal choice for ocean energy conversion systems. The only moving parts in the turbine are the rotor and generator shaft assembly. However, this turbine is hampered by poor starting performance, low efficiency, and a limited operating range. It is primarily utilized for low current speeds, such as those produced by ocean waves [8]. Wave energy systems generally have low efficiency, rendering them economically unviable. To achieve optimal performance, system components need to be redesigned.
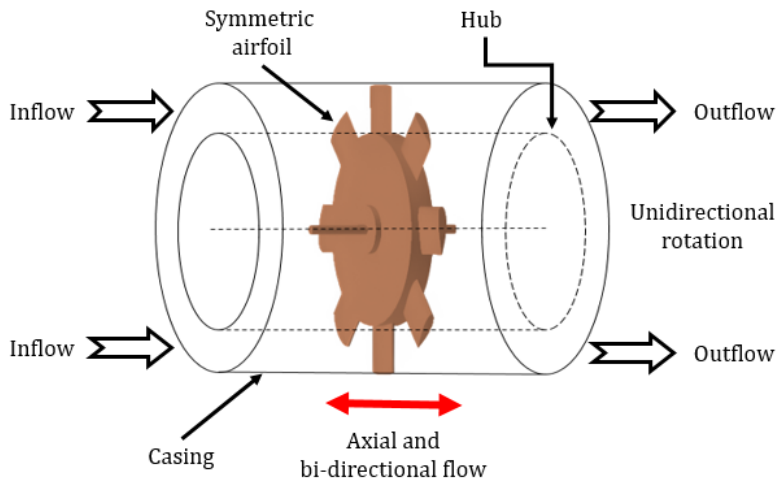

Fig. 2. Schematic of the Wells turbine

Over the past three decades, most studies on the Wells turbine's performance have relied on experimental approaches. However, a challenge arises when interpreting experimental results, as this method often lacks the capability to deliver comprehensive insights into fluid flow behavior. With advancements in computer science, computational fluid dynamics (CFD) has become a viable alternative to tackle this problem. This method offers extensive modeling capabilities for various fluid flow scenarios and has demonstrated a high level of predictive accuracy [9].

Multiple researchers have used computational fluid dynamics (CFD) to study the performance and behavior of the Wells turbine. In their work, Takao et al. [10] utilized CFD to explore the effect of adding an end plate on the overall characteristics of the turbine. Through experimental model testing under conditions of steady airflow, they aimed to quantify how the end plate influences various aspects of the turbine's operation. Similarly, Watterson and Raghunathan [11] focused their attention on understanding the role of solidity in the performance of a Wells turbine, specifically one equipped with a NACA0015 blade profile. They conducted simulations to assess how changes in the solidity, or the ratio of the blade area to the total rotor area, affected the turbine's performance and power conversion capacity.

Halder et al. [12] expanded on this by investigating how tip clearance (TC), which refers to the small gap between the rotor blades and the casing, along with the modification of grooves on the blades, influences turbine performance. Their research also employed the NACA0015 blade profile, and they found that both these design factors could significantly impact the flow characteristics and performance of the turbine. Meanwhile, Kim et al. [13] explored the effects of blade geometry on performance, specifically analyzing the relationship between the hub-to-tip ratio and the aspect ratio of the blades. Their study aimed to identify the optimal blade geometry for maximizing turbine efficiency and performance, using the NACA0020 blade profile. In this research, they kept several key parameters constant across their simulations, including the rotor aspect ratio, the solidity, the Reynolds number, and the blade sweep ratio (which is the change in the blade's chord length along its span), which characterizes the flow conditions around the blades.

Building on the previous work, the present study conducts a comprehensive numerical investigation to assess how varying the chord length of the turbine blades impacts the overall performance of the Wells turbine. The numerical simulations are based on solving the three-dimensional Reynolds-averaged Navier–Stokes (RANS) equations, which describe the fluid flow around the blades, assuming incompressible flow. A turbulence model is also employed to account for the effects of turbulence in the flow. This approach allows for a detailed analysis of the aerodynamic behavior of the turbine under different operating conditions.

In the next phase of the study, the results from the numerical simulations are validated by comparing them to experimental data obtained from previous research. This step is critical to ensure that the model provides accurate and reliable predictions that reflect the real-world performance of the Wells turbine. The validation process confirms that the model captures the key factors influencing the turbine's operation, such as the impact of chord length on the overall performance. Following the grid independence study, which ensures that the simulation results are not influenced by the resolution of the

computational grid, simulations are conducted on different turbine designs with varying chord lengths. The results of these simulations are then compared with the findings of Torressi et al. [3].

2. WELLS TURBINE PARAMETERS

The distinctive feature of the Wells turbine lies in its ability to induce unidirectional rotor rotation, a process that occurs without the need for a rectifying valve. This unique characteristic is achieved through the oscillating airflow, which plays a key role in the turbine's operation. Four-digit NACA profiles (ABXX) are commonly used to identify it [14, 15]. Three parameters shape the NACA four-digit profiles: the camber (A), the camber position (B), and the thickness as a percentage of the chord length (XX). When the first digit (A) and the second digit (B) are equal to 0, the profiles are symmetrical.

In this study, we used NACA0015. This means that the camber is 0%, the position of the maximum camber is 0%, and the thickness is 0.15 of the chord length (see in Fig. 3) [16].
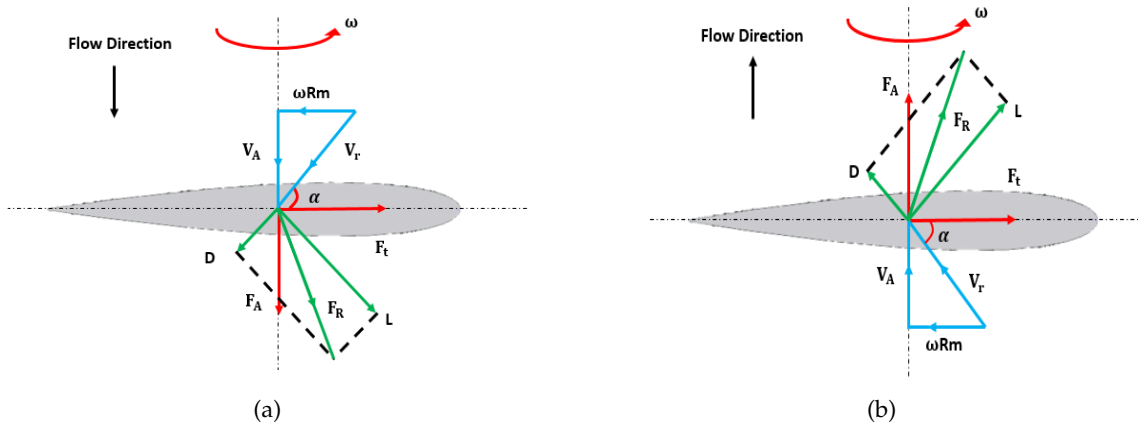

(a)   (b)

Fig. 3. Aerodynamic forces acting on a blade of the Wells turbine rotor

According to classical airfoil theory, an airfoil interacting with a fluid flow generates lift that is directed perpendicular to the freestream, while also producing drag that acts along the direction of the flow. This is illustrated in Figs. 3(a) and 3(b). As the angle of attack increases in typical fluid conditions, both lift and drag forces also rise. However, this relationship holds true only up to a certain limit. Once this limit is surpassed, the flow around the airfoil begins to separate from its surface, leading to a significant change in aerodynamic performance. The angle of attack at which this flow separation occurs is

referred to as the stall angle [17]. Beyond this stall angle, the airfoil experiences a substantial reduction in lift, while drag increases dramatically, reducing the overall efficiency of the airfoil in generating lift [18, 19].

When examining airfoils arranged in a cylindrical or linear cascade, the flow dynamics between adjacent blades can be notably different compared to isolated airfoils. This is due to the fact that the flow around each individual blade is influenced by the presence of neighboring blades. The interaction between the blades creates interference effects, which alters the airflow and leads to changes in the lift and drag characteristics for the entire cascade. As a result, the aerodynamic behavior of the cascade differs significantly from that of isolated airfoils, with both the lift and drag forces being modified due to the combined effects of the blades on the surrounding flow field [18, 19].

The Wells turbine operates in two distinct phases that are determined by the behavior of the Oscillating Water Column (OWC). The first phase is referred to as the suction stage, which occurs when the water level drops, causing air to be drawn into the turbine's duct. During this stage, the analysis of the turbine's velocity and force characteristics is similar to that shown in Fig. 3(a), where the fluid flow interacts with the airfoils in a specific manner. The second phase is known as the compression stage, which happens when the water level inside the housing rises. During this phase, as illustrated in Fig. 3(b), the flow conditions change, influencing the turbine's performance and the forces acting on the blades in a distinct way. The resultant aerodynamic forces (F_R) generated by lift (L) and drag (D) during these stages are determined by

$$F_R = \sqrt{L^2 + D^2}.$$

Decomposed in terms of lift and drag components, this force can be separated into the axial force (F_A) and the tangential force (F_t) according to the two equations below

$$F_A = L \cos \alpha + D \sin \alpha,$$

$$F_t = L \sin \alpha - D \cos \alpha,$$

where $\alpha = \tan^{-1}(U^*)$ is the angle of attack, and the force components measured in Newtons (N).

Figs. 3(a) and 3(b) also show that the tangential force maintains its direction in both stages, whereas the axial force changes direction. In the case where the airfoil parameters are designated as symmetrical, the direction of the tangential force remains the same for both positive and negative values of the angle of attack. These airfoil blades are positioned around a rotational axis. The rotor spins in the direction of the tangential force during both the upward and downward strokes, independent of the airflow direction.

The performance of the turbine can be described using four dimensionless coefficients, which assess its behavior under steady flow conditions. These coefficients are:

- The torque coefficient T^*

$$T^* = \frac{T}{\rho \omega^2 R_t^5},$$

in which ω is the angular velocity of the rotor (rad/s), ρ is the density of the air (kg/m^3), R_t is the blade tip radius (mm), and T is the turbine's shaft torque (Nm).

- The static pressure drop coefficient ΔP^*

$$\Delta P^* = \frac{\Delta p}{\rho \omega^2 R_t^2},$$

in which Δp represents the total pressure drop between the inlet and outlet of the computational domain (Pa).

- The turbine efficiency η

$$\eta = \frac{T\omega}{Q\Delta p},$$

in which Q is the volume flow rate (m^3/s).

- The flow coefficient U^*

$$U^* = \frac{U_A}{U_{tip}},$$

in which U_{tip} is the blade tip velocity (m/s), U_A is the inlet axial velocity (m/s).

3. DESCRIPTION OF THE SUGGESTED DESIGN BLADE

The geometric parameters of the baseline blade design, derived from the Islay Wells air turbine [7], are provided in Table 1. These parameters include a chord length of 125 mm for the NACA0015 blade profile shown in Fig. 4, which has been experimentally tested previously. These parameters are commonly used in many other studies investigating the performance of Wells turbines, ensuring the comprehensive collection of necessary design parameters and providing a high level of reliability for the baseline data [7,8,12,20,21].

Previous studies and experiments have shown that the efficiency of the Wells turbine increases as the flow coefficient reaches a specific value, after which it begins to decrease. When the flow coefficient exceeds a certain value, it can lead to a condition known as stall. This is due to flow separation around the turbine blades. The solidity of the turbine, s, is a parameter considered as a measure of the blockage of the airflow within the turbine [22] and also affects the efficiency of the Wells turbine

$$s = zc/\pi R_t(1+h),$$

in which z, c, R_t, and h are the number of blades, chord length, tip radius, and hub to tip ratio, respectively.

Table 1. Geometric details of the baseline turbines [3]

Blade profile	NACA0015
Number of blades (z)	8
Hub radius (R_h)	0.2 m
Tip radius (R_t)	0.3 m
Mean radius $(R_h + R_t)/2$	0.25 m
Hub to tip ratio (R_h/R_t)	0.6667
Chord length (c)	0.125 m
Solidity at mean radius (s)	0.6366
Tip clearance	0.00125 m
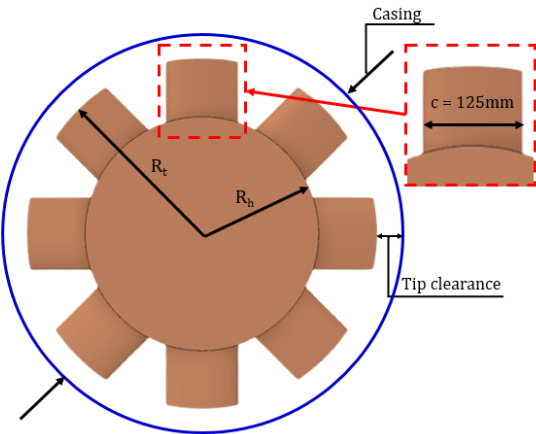
Fig. 4. Schematic view of a blade profile with the baseline turbine

As the solidity of the Wells turbine increases, which is essentially the ratio of the blade area to the total swept area of the turbine, its performance tends to decrease due to higher aerodynamic losses. This is because higher solidity leads to increased blade-to-blade interference and greater overall drag. Additionally, at higher solidity levels, significant three-dimensional effects become evident near the turbine hub. In this region, the blades are closely spaced, and their proximity causes complex interactions with the boundary layer on the hub. These interactions can result in boundary layer separation on both the hub surface and the surfaces of the adjacent blades [22]. This phenomenon is more pronounced near the hub compared to the blades tip region, where the airflow is less constrained.

Given these challenges, the paper proposes an innovative blade design approach. The design involves a blade with a chord length that varies along its span. Specifically, the chord length decreases progressively from the tip of the blade towards the hub. This variation in chord length effectively reduces the solidity s near the hub, mitigating the adverse effects caused by high blade density. The paper highlights the importance of ensuring that the turbine maintains its self-starting capability. According to the recommendations, a minimum solidity $s > 0.45$ is necessary for this purpose [23].

To achieve this, the paper suggests choosing a chord length of 0.09 m. This choice ensures that the turbine meets the required solidity criterion, balancing the need for effective performance and self-starting capability. By adopting this design, the Wells turbine can operate more efficiently, with reduced aerodynamic losses and improved overall performance, especially in regions close to the hub where three-dimensional effects are most significant.

The reduction in performance near the hub is more significant compared to near the tip of the turbine. This can be explained by the fact that, for blades with a constant chord length, the flow passage near the tip is much wider than the flow passage near the shaft [24]. When varying the chord length c, the goal is also to make the flow passage at the hub similar to that at the blade tip. This facilitates a more uniform distribution of relative velocity from the hub to the blade tip. The optimal condition is achieved when the ratio of the hub radius to the tip radius equals the ratio of the hub chord length (c_h) to the tip chord length (c_t) [24]

$$\frac{R_h}{R_t} = \frac{c_h}{c_t}.$$

Table 2. Geometric details of the suggested turbines

Blade profile	NACA0015
Number of blades (z)	8
Hub radius (R_h)	0.2 m
Tip radius (R_t)	0.3 m
Mean radius $(R_h + R_t)/2$	0.25 m
Hub to tip ratio (R_h/R_t)	0.6667
Chord length (c)	0.09 – 0.135 m
Solidity at mean radius (s)	0.57
Tip clearance	0.00125 m

Based on the previously selected c_h, the corresponding tip chord length c_t is chosen to be 0.135 m. All other parameters remain unchanged from the original model. A summary of the blade configuration and other geometric parameters is provided in Table 2. In

addition, the blade geometry for the NACA0015 blade with a chord length of 125 mm, is illustrated in Fig. 5.
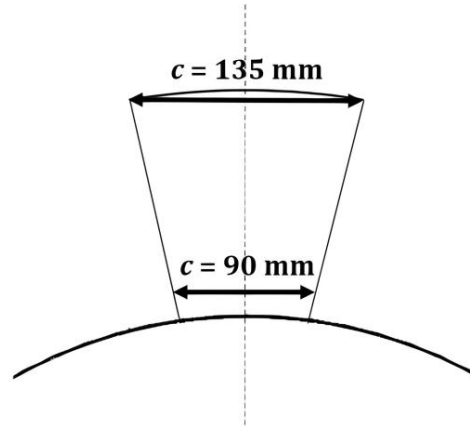

Fig. 5. Schematic view of a blade profile with the proposed turbine

4. NUMERICAL MODEL

Previous studies and experiments have shown that the efficiency of the Wells turbine increases as the flow coefficient reaches a specific value, after which it begins to decrease. When the flow coefficient exceeds a certain value, it can lead to a condition known as stall. This is due to flow separation around the turbine blades. The solidity of the turbine, s, is a parameter considered as a measure of the blockage of the airflow within the turbine [22] and also affects the efficiency of the Wells turbine. The simulations are performed using the widely recognized commercial software FLUENT, a powerful tool for computational fluid dynamics (CFD) analysis. To solve the steady-state, incompressible three-dimensional Reynolds–Averaged Navier–Stokes (RANS) equations, the finite volume method is employed. For turbulence modeling, the two-equation $k - \omega$ SST model is selected due to its proven effectiveness in managing flows characterized by adverse pressure gradients and flow separation. The $k - \omega$ SST model is a hybrid model that combines the $k - \omega$ and $k - \varepsilon$ models, effectively addressing the shortcomings of each model. Specifically, the $k - \omega$ model is used in the near-wall region to accurately capture boundary layer phenomena, while the $k - \varepsilon$ model is employed in the outer regions to mitigate the limitations that arise from the near-wall model. This dual approach ensures a more reliable representation of turbulent flows across a wide range of conditions, especially for flows with significant separation or complex turbulence characteristics [25]. In this study, the Wells turbine rotor is simulated using the Moving Reference Frame (MRF) method, which is particularly useful for modeling rotating machinery. The MRF method

allows the rotor to be modeled as a stationary reference frame while accounting for its rotational motion, thus simplifying the computational complexity involved in simulating rotating components. For numerical discretization, several schemes and algorithms are employed to ensure accuracy and stability. The standard scheme is used for pressure discretization, providing a straightforward approach for solving the pressure field. The SIMPLE algorithm is applied for pressure-velocity coupling, which is essential for ensuring that the velocity field and pressure field are consistent in the incompressible flow regime. Additionally, the second-order upwind scheme is utilized for discretizing the momentum, kinetic energy, and turbulence dissipation rate equations, offering improved accuracy compared to first-order schemes, especially for flows involving large gradients or sharp changes in velocity.

The computational domain for the turbine simulation takes advantage of the turbine's rotational symmetry, modeling only one-eighth of the flow annulus. Periodic boundary conditions are applied in the circumferential direction to accurately represent the full turbine geometry. The flow domain dimensions are defined based on established guidelines from the literature. Specifically, the upstream length is set to four times the chord length and the downstream length is set to six times the chord length, as recommended by [3, 12].
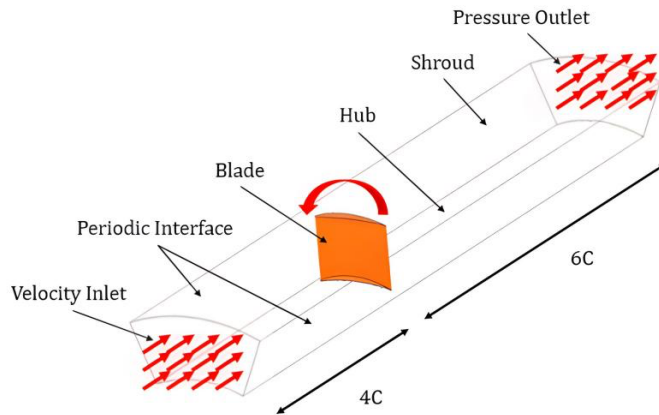

Fig. 6. The computational flow domain with the blade

Fig. 6 provides a perspective view of the computational domain. The domain is discretized using an unstructured tetrahedral mesh created in Fluent Meshing. The mesh consists of around one million cells, allowing for an accurate and detailed representation of the flow. To accurately resolve the boundary layer near the blade, prism layers are added to the mesh. The prism layers are set with an initial height of 0.01 mm and a growth ratio of 1.15, which enhances the refinement of the boundary layer and improves the accuracy of the simulation results (see in Fig. 7).
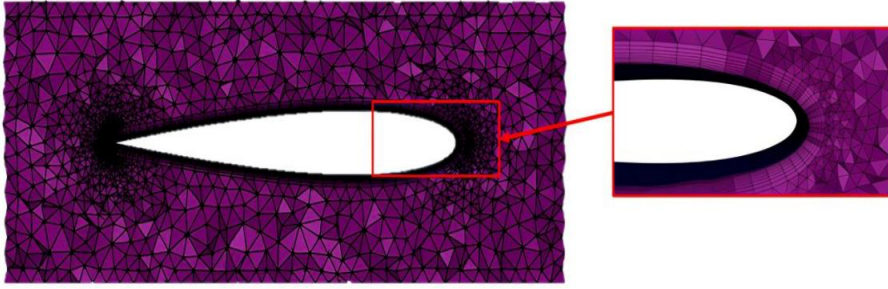
Fig. 7. Discretized computational domain

Assuming a constant angular velocity of $\omega = 2000$ rpm, the turbine operates under these conditions. The simulations are performed for 5 different cases under steady flow conditions, with the flow coefficient varying from $U^* = 0.075$ to $U^* = 0.275$. The flow coefficient is adjusted by maintaining a constant the blade tip velocity and varying the inlet velocity in each case. Table 3 provides the variation in the flow coefficient values corresponding to different inlet velocities.

Table 3. Flow coefficient and inlet axial velocity

U^*	U_A (m/s)
0.075	4.712
0.125	7.854
0.175	10.996
0.225	14.137
0.225	17.279

The boundary conditions applied are:

- No-slip boundary conditions are applied at the blade surface, hub, rotor, and casing.

- Periodicity conditions are enforced along the meridional surfaces, with a $45°$ spacing in the tangential direction.

- At the inflow surface of the annulus, a uniform velocity profile is specified.

- At the outflow surface of the annulus, simple radial equilibrium is applied.

The simulations are conducted using double precision to reduce round-off errors and ensure higher numerical accuracy. Convergence is achieved by setting the root mean square (RMS) of the residuals to 1e−5 and the mass imbalance to 0.005%, ensuring the stability and accuracy of the simulation results.

5. RESULTS AND DISCUSSION

5.1. Grid dependency and validation

To ensure the accuracy of the CFD simulation results, it is crucial to perform a grid independence test and compare the findings with current data. This helps to verify the reliability of the numerical model. To ensure numerical accuracy, the mesh is assessed for pressure drop convergence. As shown in Fig. 8, the grid independence test was conducted using various grid sizes at the same flow coefficient, leading to the selection of an optimal grid count of 1,617,071 cells. However, due to the complexity of the tip region, using a fixed number of cells or elements for all designs is not feasible. The mesh needs to be adapted to the specific geometry of each design.
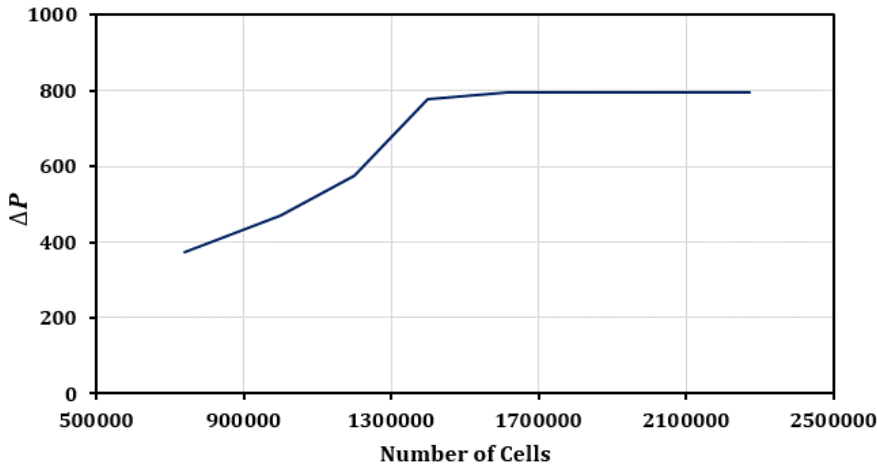
Fig. 8. ΔP results with respect to different grid numbers

For verification of the numerical methodology's accuracy, a comparison is made between the current results, experimental data from [7], and numerical results from [3,12]. The non-dimensional performance parameters T^*, ΔP^*, and η are charted against U^*. To cover the full spectrum of flow conditions, the inlet axial velocity U_A ranging from 4.712 to 17.279 (m/s). Fig. 9 demonstrates that the current numerical results closely match the available experimental and numerical data. The pressure drop coefficient in the current results remains linearly related to the flow coefficient, similar to the previous results. As the flow coefficient increases, the pressure drop coefficient also rises. As U^* increases from 0.075 to 0.225, torque coefficient gradually increases. At $U^* = 0.225$, the system reaches the stall point, after which both torque coefficient and efficiency decrease sharply as a result of flow separation.
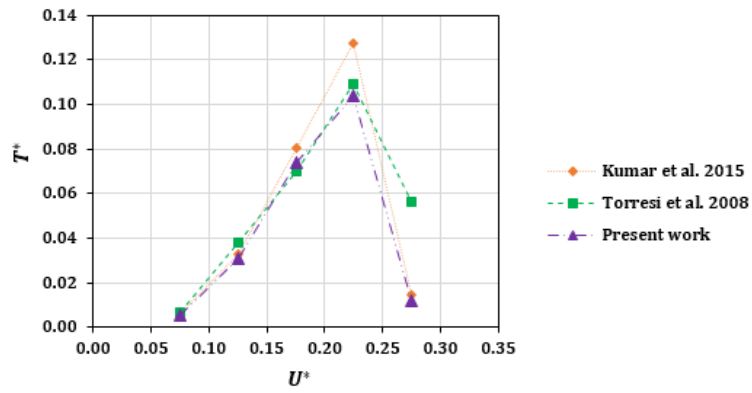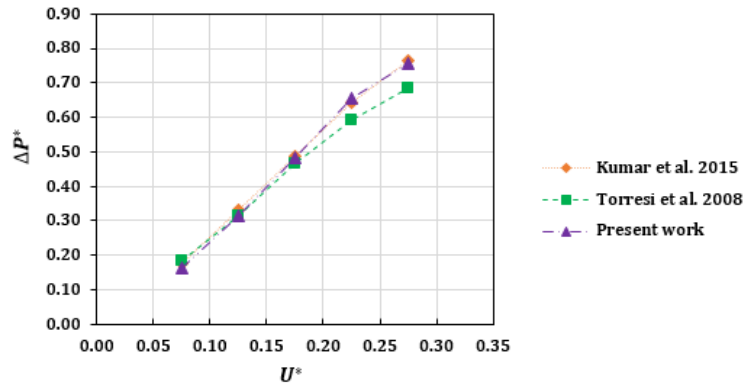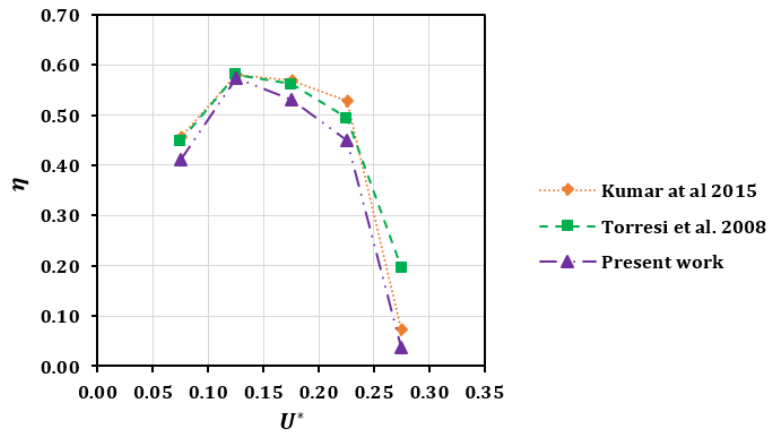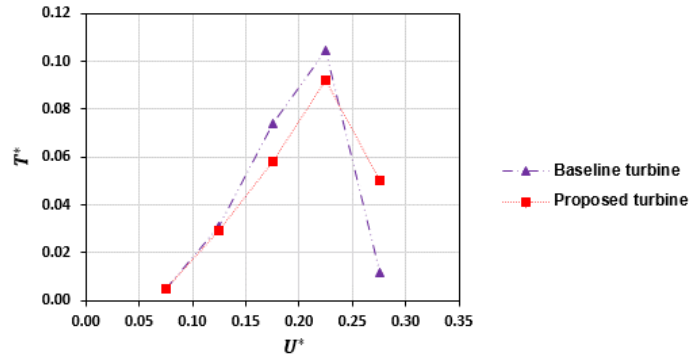
(a) Torque coefficient, T^*

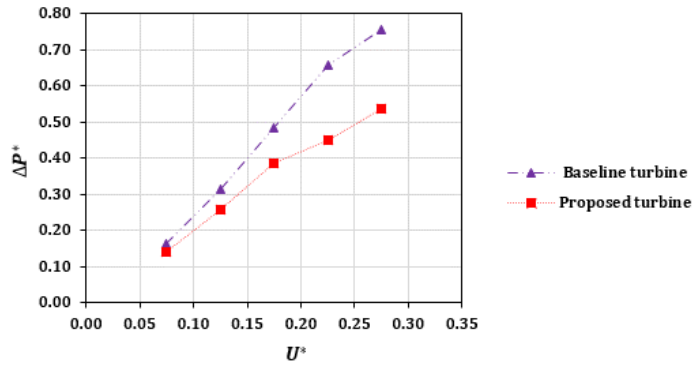(b) Static pressure drop coefficient, ΔP^*

(c) Efficiency, η

Fig. 9. Validation with experimental and numerical results

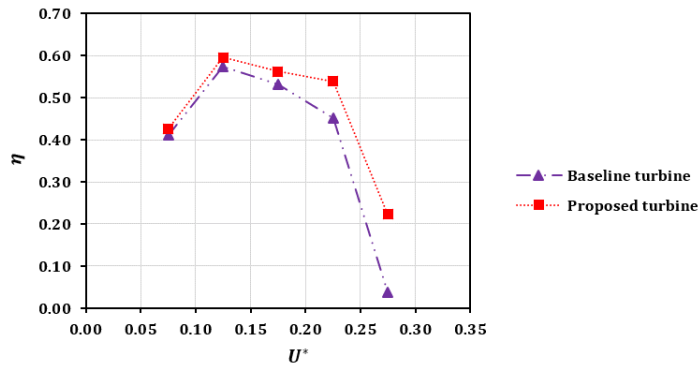## 5.2. Effect of chord length on the turbine performance

The static pressure drop coefficient, torque coefficient and efficiency of the proposed turbine with variable chord length and the baseline turbine with constant chord length are shown in Fig. 10.

(a) Torque coefficient, T^*

(b) Static pressure drop coefficient, ΔP^*

(c) Efficiency, η

Fig. 10. Comparative study of baseline turbine and proposed turbine

Despite the differences in chord length configuration, the variation patterns of these performance parameters follow similar trends for both turbines. As shown in Fig. 10(a), the overall torque coefficient of the proposed turbine is lower than that of the baseline turbine. However, from Fig. 10(a), it can be seen that the proposed turbine has delayed the stall process; at the stall point of both turbine, the torque of the proposed turbine tends to decrease more slowly than that of the baseline turbine. At $U^* = 0.275$, while the baseline turbine appears to have stalled, the T^* of the proposed turbine remains relatively high. From Fig. 10(b), the pressure reduction coefficient maintains a linear relationship with the flow coefficient; the proposed turbine has significantly reduced the pressure reduction coefficient. The efficiency of the turbine is compared in Fig. 10(c); where it is observed that the overall efficiency of the turbine increases by 33%, reaching the maximum efficiency of 59.6% at $U^* = 0.125$. Additionally, to gain a deeper understanding of the aerodynamic performance of the proposed turbine and the baseline turbine under different flow conditions, in-depth flow analyses need to be conducted.
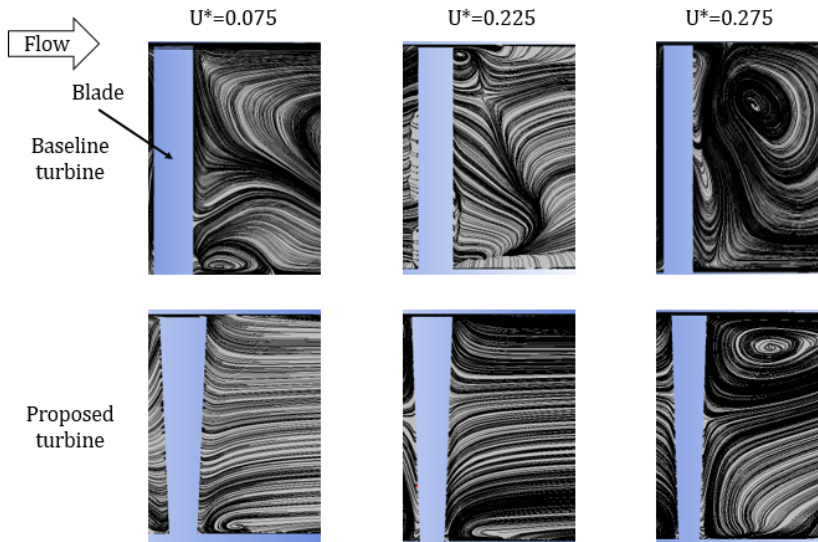

Fig. 11. Streamline at mid-chord locations

Fig. 11, the flow through the turbine blades at the mid-chord section is shown. At $U^* = 0.075$, a small counter-clockwise vortex is observed in the hub region for both the baseline and proposed turbines. However, the vortex in the proposed turbine is smaller, and the flow continues to follow the blade surface, whereas the baseline turbine begins to exhibit flow separation. As the flow coefficients increase to 0.225, the flow through the proposed turbine remains relatively unchanged and stable, while in the baseline turbine, the previously observed vortex develops into a more pronounced flow separation region, indicating that the turbine reaches the stall point, and an additional clockwise

vortex appears near the tip. This vortex grows and completely covers the blade span of the baseline turbine when the flow coefficients reach 0.275, at which point the baseline turbine has entered a deep stall state. At this time, the proposed turbine also shows a vortex near the tip, but overall, the flow separation is still not as pronounced. From Fig. 11, it can be observed that the variation in chord length decreasing towards the hub facilitates flow distribution, particularly for high-speed flow conditions, thereby delaying the onset of stall in the turbine.
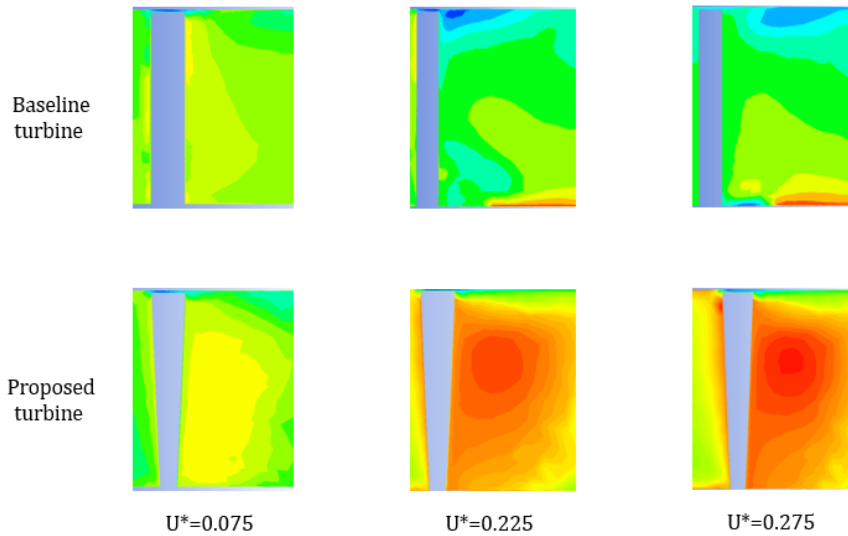

Fig. 12. Tangent velocity contours at mid-chord locations

Fig. 12 illustrates the tangential velocity contours at the mid-chord section. Firstly, it can be observed that the tangential velocity of the proposed turbine is higher than that of the baseline turbine, with this improvement being more pronounced at $U^* = 0.225$ and $U^* = 0.275$. The tangential velocity field of the proposed turbine is uniformly distributed across the entire span and is enhanced as the flow coefficient increases. Both types of blades exhibit regions of low tangential velocity at the blade tip surface, known as tip leakage flows. The cause of this leakage is the pressure difference between the pressure and suction surfaces at the blade tip. As the flow coefficient increases, the tip leakage flows grow in size, resulting in turbulence and causing the flow to detach from the main flow. This results in increased blockage and reduced turbine performance. For the baseline turbine, tip leakage flows develop rapidly with an increase in the flow coefficient, adversely affecting the tangential velocity distribution and causing flow separation that leads to increased blockage. In contrast, the proposed turbine limits the development of tip leakage flows, reduces the interaction between these flows and the main flow, thereby improving efficiency and extending the operational range of the turbine.
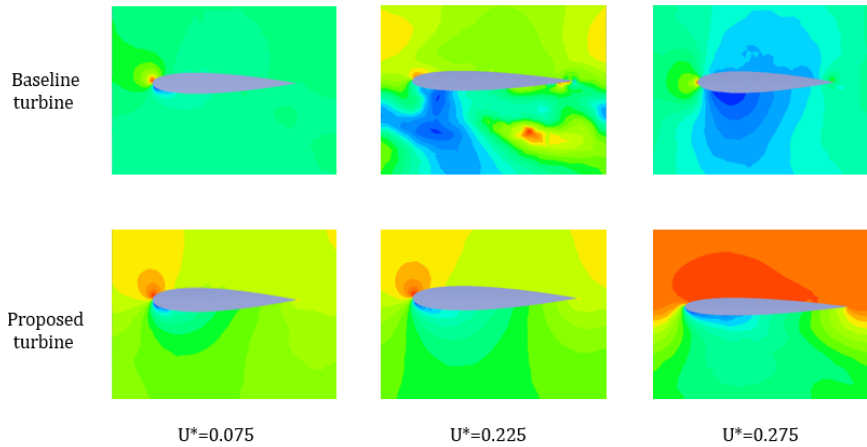
<div align="center">U*=0.075   U*=0.225   U*=0.275</div>

Fig. 13. Static pressure coefficient contours at midspan locations

Fig. 13 shows a comparison of the static pressure coefficient of the flow passage between the baseline turbine and the proposed turbine at the mid-section. At a low flow coefficient of $U^* = 0.075$, the static pressure on both the pressure and suction surfaces of the turbines remains relatively constant for both types of turbines. In this condition, only a small low-pressure region is observed near the leading edge. This low-pressure area creates conditions that favor flow separation, which ultimately results in a reduction in turbine efficiency. As the flow coefficient increases, a noticeable trend is observed where the static pressure coefficients also rise. At a flow coefficient of $U^* = 0.225$, the low-pressure region expands significantly, covering approximately 80% of the suction surface for the baseline turbine, while it affects around 60% of the suction surface for the proposed turbine. In this case, the baseline turbine shows a more pronounced development of a large vortex near the leading edge, which further contributes to the flow separation and loss of performance. When the flow coefficient increases to $U^* = 0.275$, the low-pressure region grows even more. For the proposed turbine, this region now covers roughly 80% of the suction surface, while for the baseline turbine, the low-pressure area almost entirely engulfs the suction surface. This further intensifies the conditions that lead to flow separation, resulting in a stall condition for the baseline turbine. As a consequence, the efficiency of the proposed turbine experiences a significant decline under these conditions.

In summary, as the flow coefficient increases, both turbines exhibit a growing low-pressure region that promotes flow separation. However, the baseline turbine is more susceptible to flow instabilities, resulting in a more severe stall condition and greater efficiency loss compared to the proposed turbine.

6. CONCLUSIONS

An optimal performance design of the Wells turbine is proposed by varying the chord length gradually towards the hub. Its aerodynamic performance has been computed numerically. The results obtained from the calculations and analysis indicate that the turbine with the proposed design exhibits better performance and enhanced operational range compared to the baseline turbine. Additionally, several in-depth flow analyses, including flow field, tangential velocity, and static pressure coefficient, are conducted to further elucidate the impact of chord length on the aerodynamic performance of the Wells turbine. The key findings of this study are:

- The torque coefficient and pressure drop coefficient both decrease across the entire flow coefficient range.

- The maximum efficiency achieved is 59.6%, an increase of 3.8% over the baseline turbine, with the overall efficiency in the computed range ($0.075 \leq U^* \leq 0.275$) improving by 33%. At the same time, the operational range is relatively enhanced.

- The improved performance is attributed to the reduction in flow separation, limitation of the spread of tip leakage flows, and decreased impact on the main flow.

DECLARATION OF COMPETING INTEREST

The authors declare that they have no known competing financial interests or personal relationships that could have appeared to influence the work reported in this paper.

ACKNOWLEDGEMENT

REFERENCES

[1] The Department of Business, Economic Development, and Tourism (DBEDT). *Feasibility of developing wave power as renewable energy resource for Hawaii*, (2002).

[2] M. Amundarain, M. Alberdi, A. J. Garrido, I. Garrido, and J. Maseda. Wave energy plants: Control strategies for avoiding the stalling behaviour in the Wells turbine. *Renewable Energy*, **35**, (2010), pp. 2639–2648. https://doi.org/10.1016/j.renene.2010.04.009.

[3] M. Torresi, S. M. Camporeale, P. D. Strippoli, and G. Pascazio. Accurate numerical simulation of a high solidity Wells turbine. *Renewable Energy*, **33**, (2008), pp. 735–747. https://doi.org/10.1016/j.renene.2007.04.006.

[4] A. Clément, P. McCullen, A. Falcão, A. Fiorentino, F. Gardner, K. Hammarlund, G. Lemonis, T. Lewis, K. Nielsen, S. Petroncini, M.-T. Pontes, P. Schild, B.-O. Sjöström, H. C. Sørensen, and

T. Thorpe. Wave energy in Europe: current status and perspectives. *Renewable and Sustainable Energy Reviews*, **6**, (2002), pp. 405–431. https://doi.org/10.1016/s1364-0321(02)00009-6.

[5] M. Paderi and P. Puddu. Experimental investigation in a Wells turbine under bi-directional flow. *Renewable Energy*, **57**, (2013), pp. 570–576. https://doi.org/10.1016/j.renene.2013.02.016.

[6] A. F. O. Falcão and J. C. C. Henriques. Oscillating-water-column wave energy converters and air turbines: A review. *Renewable Energy*, **85**, (2016), pp. 1391–1424. https://doi.org/10.1016/j.renene.2015.07.086.

[7] R. Curran and L. M. C. Gato. The energy conversion performance of several types of Wells turbine designs. *Proceedings of the Institution of Mechanical Engineers, Part A: Journal of Power and Energy*, **211**, (1997), pp. 133–145. https://doi.org/10.1243/0957650971537051.

[8] A. S. Shehata, Q. Xiao, K. M. Saqr, and D. Alexander. Wells turbine for wave energy conversion: a review. *International Journal of Energy Research*, **41**, (2016), pp. 6–38. https://doi.org/10.1002/er.3583.

[9] T. H. Kim, T. Setoguchi, K. Kaneko, and S. Raghunathan. Numerical investigation on the effect of blade sweep on the performance of Wells turbine. *Renewable Energy*, **25**, (2002), pp. 235–248. https://doi.org/10.1016/s0960-1481(00)00210-x.

[10] M. Takao, T. Setoguchi, Y. Kinoue, and K. Kaneko. Wells turbine with end plates for wave energy conversion. *Ocean Engineering*, **34**, (2007), pp. 1790–1795. https://doi.org/10.1016/j.oceaneng.2006.10.009.

[11] J. K. Watterson and S. Raghunathan. Computed effects of solidity on Wells turbine performance. *JSME International Journal Series B*, **41**, (1), (1998), pp. 177–183. https://doi.org/10.1299/jsmeb.41.177.

[12] P. Halder, A. Samad, J.-H. Kim, and Y.-S. Choi. High performance ocean energy harvesting turbine design–A new casing treatment scheme. *Energy*, **86**, (2015), pp. 219–231. https://doi.org/10.1016/j.energy.2015.03.131.

[13] T. Kim, T. Setoguchi, Y. Kinoue, and K. Kaneko. Effects of blade geometry on performance of wells turbine for wave power conversion. *Journal of Thermal Science*, **10**, (2001), pp. 293–300. https://doi.org/10.1007/s11630-001-0035-4.

[14] E. N. Jacobs and A. Sherman. *Airfoil section characteristics as affected by variation of the Reynolds number*. NACA Report No. 586, (1937).

[15] R. E. Sheldahl and P. C. Klimas. *Aerodynamic characteristics of seven symmetrical airfoil sections through 180-degree angle of attack for use in aerodynamic analysis of vertical axis wind turbines*. Sandia National Laboratories energy report, (1981). https://doi.org/10.2172/6548367.

[16] S. Raghunathan, C. P. Tan, and N. A. J. Wells. Wind tunnel tests on airfoils in tandem cascade. *AIAA Journal*, **19**, (1981), pp. 1490–1492. https://doi.org/10.2514/3.60084.

[17] W. P. Wolfe and S. S. Ochs. *Predicting aerodynamic characteristic of typical wind turbine airfoils using CFD*. (1997). https://doi.org/10.2172/534484.

[18] A. Gareev, B. Kosasih, and P. Cooper. Analysis of interference factors of air turbine cascades. *Engineering Applications of Computational Fluid Mechanics*, **7**, (2013), pp. 496–506. https://doi.org/10.1080/19942060.2013.11015488.

[19] N. Scholz. *Aerodynamics of cascades*. AGARD-AG- 220. NATO Science and Technology Organization: Amsterdam.

[20] S. Shaaban and A. Abdel Hafiz. Effect of duct geometry on Wells turbine performance. *Energy Conversion and Management*, **61**, (2012), pp. 51–58. https://doi.org/10.1016/j.enconman.2012.03.023.

[21] P. Halder and A. Samad. Casing treatment of a wave energy extracting turbine. *Aquatic Procedia*, **4**, (2015), pp. 516–521. https://doi.org/10.1016/j.aqpro.2015.02.067.

[22] S. Raghunathan. The wells air turbine for wave energy conversion. *Progress in Aerospace Sciences*, **31**, (1995), pp. 335–386. https://doi.org/10.1016/0376-0421(95)00001-f.

[23] M. H. Mohamed. Aerodynamic performance of the Wells turbine used in the sea wave conversion. Master's thesis, Helwan University, Cairo, Egypt, (2003).

[24] M. H. A. Mohamed. *Design optimization of Savonius and Wells turbines*. PhD thesis, Magdeburg, Germany, (2011).

[25] F. R. Menter. Two-equation eddy-viscosity turbulence models for engineering applications. *AIAA Journal*, **32**, (1994), pp. 1598–1605. https://doi.org/10.2514/3.12149.